A Power-Efficient Switched-Capacitor Stimulating System for Electrical/Optical Deep Brain Stimulation

Hyung-Min Lee, *Student Member, IEEE*, Ki Yong Kwon, *Student Member, IEEE*, Wen Li, *Senior Member, IEEE*, and Maysam Ghovanloo, *Senior Member, IEEE*

***Abstract*—A power-efficient wireless switched-capacitor based stimulating (SCS) system for electrical/optical deep brain stimulation (DBS) is presented. The SCS system efficiently charges storage capacitors directly from an inductive link and delivers accurately balanced charge to the tissue, improving the overall stimulator efficiency. In addition, the decaying exponential stimulus pulses generated by SCS can be more effective than conventional rectangular and ramp stimuli in activating neural tissue when consuming the same amount of energy, leading to higher stimulus efficacy. A 4-channel wireless SCS system in 0.35 µm CMOS process achieves stimulator efficiency of 80.4% with capacitor pairs charged to ±2V, while the decaying exponential stimulus requires equal or less stimulus energy and injected charge than other stimuli depending on pulse width to activate the same tissue area. The SCS system has also been utilized for power-efficient wireless optogenetic stimulation by periodically discharging capacitors into high-current micro-LED arrays. Results from acute *in vivo* experiments have verified the utility of the SCS system prototype in both electrical and optical stimulation.**

***Index Terms*—Deep brain stimulation, switched-capacitor based stimulators, wireless power transfer, inductive capacitor charger, optogenetics, implantable medical devices, charge monitoring.**

I. Introduction

DEEP BRAIN STIMULATION (DBS) has been proven as an effective therapy to alleviate Parkinson's disease, tremor, and dystonia [1], [2]. Traditional DBS devices have used large primary batteries implanted in the chest area, which need to be replaced every 2–5 years through surgery [3]. Moreover, subcutaneous interconnects from batteries pass across the neck to reach the electrodes implanted deep in the brain, increasing the risk of mechanical failure due to head motion. Towards a less invasive head-mounted DBS system, we have utilized an inductive transcutaneous link to be driven by a behind the ear (BTE) rechargeable energy source, similar to cochlear implants and hearing aids, to provide sufficient power to the stimulator without size, lifetime, and discomfort of chest-mounted battery-powered traditional DBS [4], [5].

Manuscript received April 06, 2014; revised July 11, 2014; accepted September 01, 2014. Date of publication October 03, 2014; date of current version December 24, 2014. This paper was approved by Guest Editor David Stoppa.

H.-M. Lee and M. Ghovanloo are with the GT-Bionics Lab, School of Electrical and Computer Engineering, Georgia Institute of Technology, Atlanta, GA 30308 USA (e-mail: mgh@gatech.edu).

K.-Y. Kwon and W. Li are with the Microtechnology Lab, Department of Electrical and Computer Engineering, Michigan State University, East Lansing, MI 48824 USA.

Color versions of one or more of the figures in this paper are available online at http://ieeexplore.ieee.org.

Digital Object Identifier 10.1109/JSSC.2014.2355814

The next step is adopting aggressive power management schemes to further improve the DBS efficiency. Voltage-controlled stimulation (VCS) enables power-efficient stimulation. However, limiting and balancing the stimulation charge are complicated in VCS because the electrode impedance varies over time and position [6], [7]. On the other hand, current-controlled stimulation (CCS) provides precise charge control and safe operation, but it has low power efficiency due to the dropout voltage across its current sources [8], [9]. Switched-capacitor stimulation (SCS), proposed in [10], takes advantage of both high efficiency of VCS and safety of CCS using capacitor banks to transfer quantized amount of charge to the tissue. However, that was a simple presentation of the general SCS idea with no on-chip integration. It also requires an efficient capacitor charging mechanism directly from the inductive link to maintain its benefits. In this paper, we present the first integrated wireless SCS system-on-a-chip (SoC) with inductive capacitor charging and charge-based stimulation capabilities, which can improve both stimulator efficiency (before the electrodes) and stimulus efficacy (after the electrodes) in DBS.

Fig. 1 compares the key blocks involved in the inductive power flow from the external energy source to the tissue in conventional CCS and the proposed SCS systems, as well as the resulting stimulus waveforms. The CCS requires a rectifier, a regulator, and an array of current sources to generate a rectangular current stimulus. Accumulated power losses at each stage result in poor overall stimulator efficiency, which can be defined as the stimulator output power over input power from the L_2C_2 tank. On the other hand, the streamlined inductively-powered SCS efficiently charges the storage capacitors directly from the inductive link and delivers the quantized stored charge to the tissue (series *RC*), improving stimulator efficiency. In addition, the proposed SCS is capable of generating a decaying exponential stimulus by dumping the capacitor charge in the tissue without wasting additional power. The decaying exponential stimulus can be equally, if not more, effective in activating the larger target tissue area compared to the conventional rectangular or ramp stimuli while consuming the same amount of energy, improving both stimulus efficacy and safety [11], [12].

Optical stimulation of neuronal circuits, known as optogenetic stimulation, has rapidly gained popularity as an effective way to selectively activate genetically-modified neurons using various light-delivery schemes, including LEDs, because of their fast, spatially controlled, and minimally invasive modulation of activity in the targeted cell types [13], [14]. However, LEDs typically require large instantaneous power to emit sufficient light above the optical stimulation threshold, which is

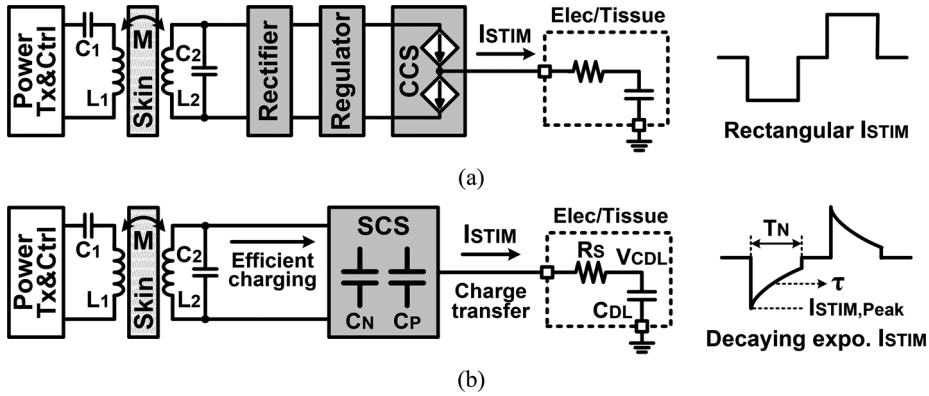

Fig. 1. Key power delivery blocks in the (a) conventional current-controlled stimulation (CCS) and (b) proposed switched-capacitor based stimulation (SCS).

a limiting factor in conventional inductively-powered devices that often have a limited continuous power stream highly dependent on the coils' coupling. Moreover, instantaneous load variations affect the matching condition, further degrading the inductive power transmission efficiency (PTE) [15], [16]. To address this limitation, we have utilized the SCS system for power-efficient optogenetics by periodically discharging the capacitors into LEDs, providing high instantaneous current to a micro-LED array.

The rest of this paper, which is an extended version of [17], focuses on detailed circuit techniques and additional measurement results to fully describe the overall SCS system, while providing stimulus waveform analysis and several *in vivo* experiment results to demonstrate both electrical and optical stimulation. Section II presents the proposed wireless SCS system and its stimulation parameter analysis. Section III describes the circuit details and design considerations, including an inductive capacitor charger, a charge monitoring circuit, and forward/back telemetry. Section IV depicts the SoC measurement results. Section V presents the SCS energy-efficient stimulus waveform with *in vivo* electrical stimulation experiments. Section VI describes wireless SCS optogenetics and its *in vivo* results, followed by concluding remarks in Section VII.

II. Wireless Switched-Capacitor Stimulating System

Fig. 2 shows the overall architecture of the wireless SCS system for head-mounted DBS. The inductive capacitor charger, adopted and improved from [21], charges four pairs of positive/negative storage capacitors, $C_{P1\sim4}$ and $C_{N1\sim4}$, sequentially, while the adaptive capacitor tuner compensates for the resonance capacitance variation during charging [21]. These capacitors deliver charge to the stimulation sites, which can be either microelectrode arrays (MEA) or micro-LED arrays, through capacitor/channel selectors for electrical or optical stimulation, respectively. The capacitor and channel selectors, which consist of low-resistance switches to minimize the power loss and impact on the stimulus shape, control the connections between storage capacitors and stimulation channels. For biphasic electrical stimulation, the capacitor pairs are alternately connected to the electrodes, dumping negative and positive charge to the tissue. A current limiter limits the stimulus amplitude to prevent large current flowing through the tissue. To ensure charge-balanced stimulation, a charge monitoring circuit measures the amount of charge injected and withdrawn by observing storage capacitor voltages, and dynamically changes the stimulus pulse width to neutralize the residual charge in the tissue. An additional charge balancing circuit further prevents residual charge accumulation by shorting electrodes to ground for a predefined time after stimulation. A power management block, similar to [21], generates system supply and reference voltages, while a timing controller provides timing signals for capacitor charging and charge-based stimulation.

For forward data telemetry, a pulse-position-modulated clock and data recovery (PPM-CDR) block extracts synchronized data and clock from an on-off-keying (OOK) modulated coil voltage, V_{COIL}, setting a 40 bit shift register through a serial-to-parallel converter (S2P) with an 8 bit preamble, to store stimulation parameters. Back telemetry through load-shift-keying (LSK) has been adopted for handshaking during forward telemetry and establishing a closed-loop power control mechanism by sensing rectifier output voltage, V_{REC}, which discrete implementation was introduced in [18].

The decaying exponential shape of the current stimulus can be adjusted by changing the stimulation parameters that are set through forward telemetry. We analyze the decaying exponential current stimulus with the simplified SCS system and electrodes/tissue model, as shown in Fig. 1(b). The electrodes/tissue model includes a series R_S and C_{DL}, which represent the solution spreading resistance and the double-layer capacitance, respectively [19], [20].

Here we assume that storage capacitors, C_N and C_P, are charged to target voltages, V_{TN} and V_{TP}, respectively, and C_{DL} is discharged to 0 V. When C_N is connected, the stimulation current, I_{STIM}, flows to the tissue through electrodes. During the negative stimulation (cathodic) phase, V_{CN}, V_{CDL}, and I_{STIM} can be expressed as

$$\mathrm{V_{CN}}(t) = \mathrm{V_{TN}} - \frac{1}{\mathrm{C_N}} \int \mathrm{I_{STIM}}(t)\,\mathrm{d}t \tag{1}$$

$$\mathrm{V_{CDL}}(t) = \frac{1}{\mathrm{C_{DL}}} \int \mathrm{I_{STIM}}(t)\,\mathrm{d}t \tag{2}$$

$$\mathrm{I_{STIM}}(t) = \frac{\mathrm{V_{CN}}(t) - \mathrm{V_{CDL}}(t)}{\mathrm{R_S}} = \frac{\mathrm{V_{TN}} - \left(\frac{1}{\mathrm{C_P}} + \frac{1}{\mathrm{C_{DL}}}\right) \int \mathrm{I_{STIM}}(t)\,\mathrm{d}t}{\mathrm{R_S}} \tag{3}$$

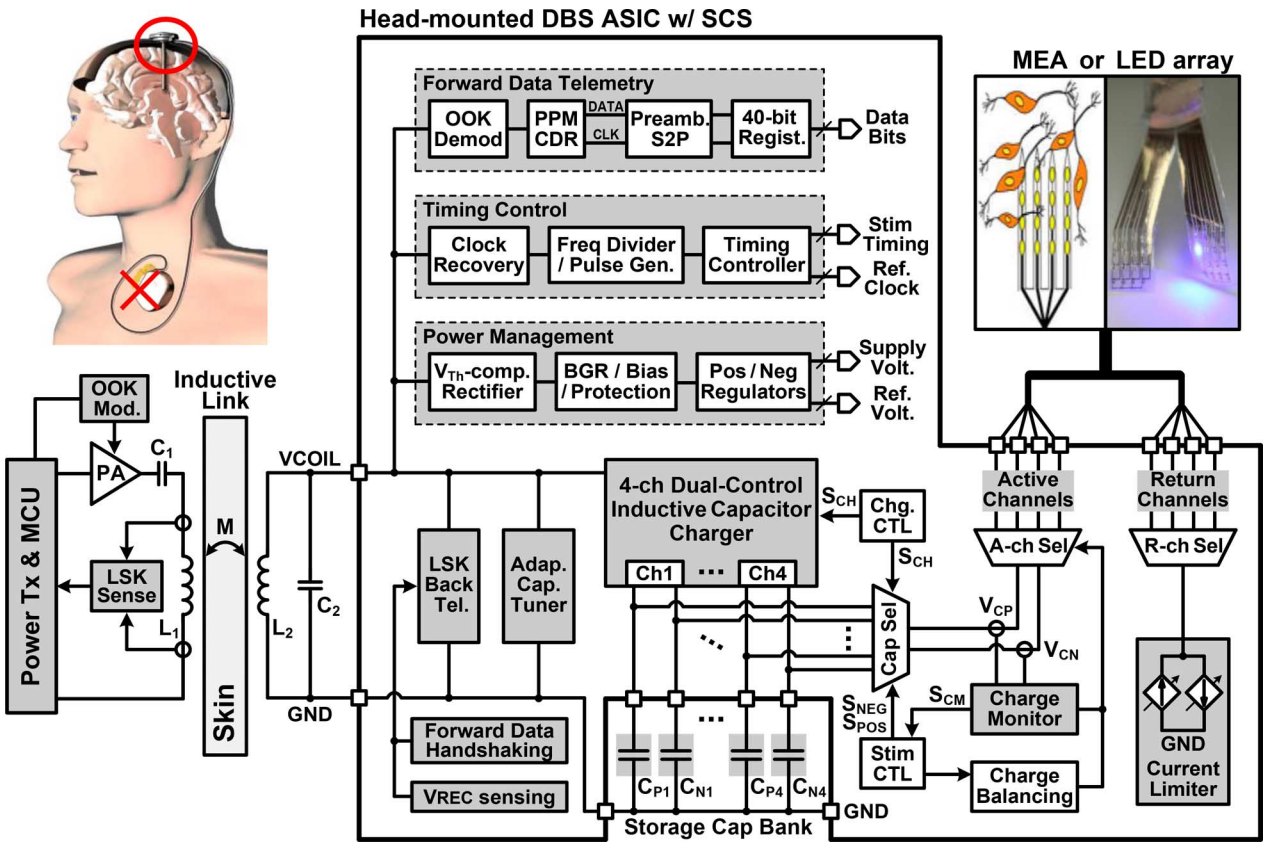

Fig. 2. Overall architecture of the integrated wireless SCS system for head-mounted DBS.

Then, I_{STIM} can be derived further as

$$\begin{aligned} \mathrm{I_{STIM}}(t) &= \frac{\mathrm{V_{TN}}}{\mathrm{R_S}} \exp\left(-\left(\frac{1}{\mathrm{C_P}}+\frac{1}{\mathrm{C_{DL}}}\right)\left(\frac{1}{\mathrm{R_S}}\right)t\right) \\ &= \frac{\mathrm{V_{TN}}}{\mathrm{R_S}} \exp\left(-\frac{\mathrm{t}}{\frac{\mathrm{C_P C_{DL}}}{\mathrm{C_P+C_{DL}}}\mathrm{R_S}}\right) \\ &= \frac{\mathrm{V_{TN}}}{\mathrm{R_S}} \exp\left(-\frac{\mathrm{t}}{\tau}\right) \end{aligned} \tag{4}$$

From (4), the peak stimulation current, $I_{STIM,Peak}$ $(=V_{TN}/R_S)$, and the time constant of decaying exponential, τ, can be partially adjusted by changing the target charging voltage, V_{TN}, and the number of storage capacitors connected in parallel to the tissue $(=C_N \times n)$, respectively. The cathodic phase period, T_N, can also be controlled through forward telemetry, enabling flexible shapes of decaying exponential current stimulus, as shown in Fig. 1(b). The positive stimulation (anodic) phase current can be adjusted in the same way with V_{TP}, C_P, and T_P parameters. Since the stimulus shape is also affected by R_S and C_{DL}, it is required to know the impedance range of the electrode and tissue interface to estimate the peak amplitude and time constant of decaying exponential stimuli generated by the SCS system.

III. Circuit Details and Design Considerations

A. Inductive Capacitor Charger

Since capacitor charging efficiency is a dominant factor in the overall stimulator efficiency, we utilized the power-efficient inductive capacitor charging mechanism in [21] plus two newly added safety features for the SCS application. These features are the dual-voltage control capability and optional reset function. Fig. 3 shows the schematic diagram of the improved 4-channel inductive capacitor charger. One of the receiver coil terminals, V_{COIL}, is followed by a series charge injection capacitor, C_S, which provides an input voltage, V_{IN}, to C_{P1} and C_{N1} through switches $\mathrm{P_1}$ and $\mathrm{N_1}$, respectively. C_{P1} and C_{N1} are alternately charged depending on V_{COIL} variations as shown in Fig. 4. For example, when V_{COIL} increases and V_{IN} is less than V_{CP1}, both switches are off, and V_{IN} follows V_{COIL}. When V_{IN} exceeds V_{CP1}, $\mathrm{P_1}$ turns on by its active switch driver, $\mathrm{DRV_P}$, and connects V_{IN} to C_{P1}, holding V_{IN} relatively constant around V_{CP1}. Since V_{COIL} keeps increasing, the voltage difference across C_S generates a relatively constant charging current, I_{CH}, into the positive storage capacitors,C_{P1}. In other words, C_S operates like a current source and charges C_{P1} without dissipating power. The negative storage capacitor, C_{N1}, is charged the same way when V_{COIL} decreases. This reduces the switching loss that would otherwise result from charging a capacitor with a voltage source and significantly improves the capacitor charging efficiency through an inductive link [22]. Moreover, the control circuitry for the charger consumes a negligible amount of power

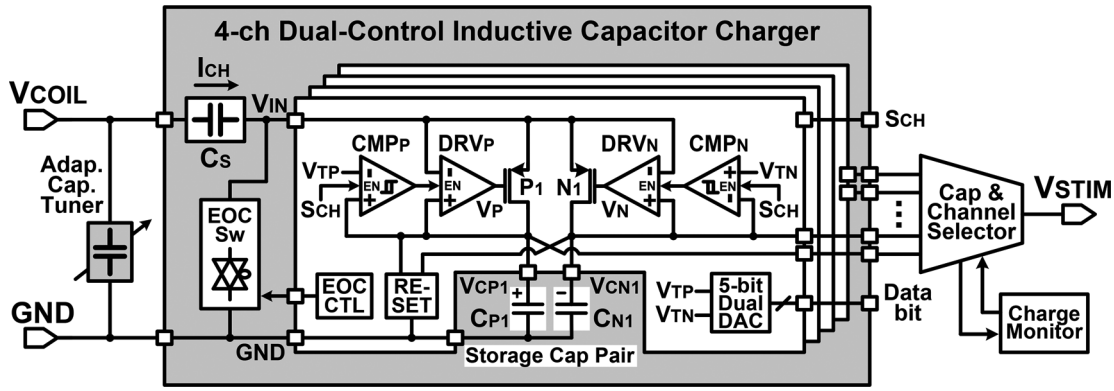

Fig. 3. Schematic diagram of the 4-channel dual-control inductive capacitor charger.

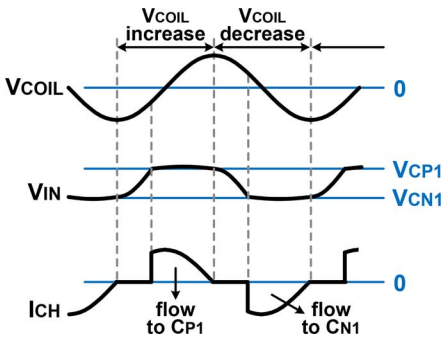

Fig. 4. Simplified voltage and current waveforms for capacitor charging.

compared to high capacitor charging power because it mainly operates in a digital mode with very small static current.

The improved charger benefits from the additional safety features, dual-voltage control capability provided by comparators, $\mathrm{CMP_P}$ and $\mathrm{CMP_N}$, and a 5 bit dual-output DAC to guarantee that V_{CP1} and V_{CN1} are separately charged to reach their target voltages, V_{TP} and V_{TN}, respectively. Otherwise, even small residual voltage mismatch between C_{P1} and C_{N1} can be accumulated over long-term stimulation periods and saturate either V_{CP1} or V_{CN1}. There is also a reset function that can optionally discharge C_{P1} and C_{N1} before charging. While the 4-channel capacitor charger operates sequentially, the end-of-charge (EOC) switch connects V_{IN} to *GND* after charging. In addition, the adaptive capacitor tuner, adopted from [21], automatically compensates for variations of the secondary resonance capacitance during charging.

B. Charge Monitoring Circuit

For accurately charge-balanced biphasic stimulation, we have utilized the charge monitoring circuit shown in Fig. 5. This circuit utilizes a capacitive-feedback amplifier to integrate the discharged voltage variations from storage capacitor voltages, V_{CP} and V_{CN}, during stimulation to detect the amount of negative and positive charges transferred to tissue. A charge monitoring signal, S_{CM}, stays at 0 before stimulation, while amplifiers $\mathrm{A_1}$ and $\mathrm{A_2}$ operate as buffers, storing their offset voltages in C_5. When the negative stimulation starts first with S_{CM} at 1 for a predefined period, $\mathrm{A_1}$ becomes a capacitive-feedback amplifier, and $\mathrm{A_2}$ operates as a comparator, while their offsets are cancelled through C_5. The sensing voltage, V_{SEN}, decreases as V_{CN} increases in this period. When V_{CP} discharges for positive stimulation, V_{SEN} increases again. When the amounts of V_{SEN} decrement and increment are equal, S_{CM} becomes 0 again, and the positive stimulation stops to ensure that the net injected and withdrawn charges are zero.

C. Forward/Back Data Telemetry

Fig. 6 shows the schematics of the OOK demodulator and PPM-CDR circuit. In the OOK demodulator, V_{COIL} is converted to a half-wave through $\mathrm{P_2}$ and $\mathrm{P_3}$ to prevent overvoltage across a following diode-connected rectifying transistor, $\mathrm{P_4}$. Then, the envelope of V_{COIL} is extracted through $\mathrm{P_4}$ and a hysteresis comparator, $\mathrm{A_3}$, to provide a pulse-position-modulated (PPM) signal, S_{PPM}. In the PPM-CDR, S_{PPM} is converted to the clock signal, *CLK*, after passing through a frequency divider $(\mathrm{DFF_1})$. *CLK* controls the timing and amplitude of V_{PPM} by alternately charging and discharging C_7 through current sources, I_2 and I_3, respectively. If positioning ratio among three pulses of S_{PPM} is 7:3, I_2 charges C_7 for longer time, and V_{PPM} exceeds a reference voltage, V_{REF2}, during $CLK = 1$. Then, a demodulated signal, S_{PPD}, is sampled in $\mathrm{DFF_2}$, leading to $DATA = 1$. On the contrary, when the positioning ratio is 3:7, V_{PPM} does not reach to V_{REF2} during $CLK = 1$, resulting in $DATA = 0$. Since the stimulation parameters are set only once and the OOK pulse width is narrow (3 μs), the OOK-PPM offers a simple but robust programming method without significantly affecting the system power efficiency.

In addition, the LSK back telemetry has been utilized for the closed-loop power control to accommodate with a wider range of mutual coil arrangements. An external power transmitter (Tx) in Fig. 2 increases the transmitted power by default with an adjustable step size unless detecting the back telemetry data. Then, the V_{REC} sensing circuit in Fig. 7 compares a portion of positive rectifier output voltage, V_{RECP}, from the power management block to a reference voltage, V_{REF3}. When V_{RECP} exceeds a certain threshold, the sensing block sends short (1.5 μs) back telemetry pulses, S_{BT}, to the LSK block at 500 Hz, closing the switch across the secondary coil, L_2. The resulting voltage increment across the primary coil, L_1, is detected by the external LSK sensing block, and the power Tx adaptively decreases the transmitted power until no more back telemetry pulses are received. This will keep V_{COIL} amplitude and rectifier output

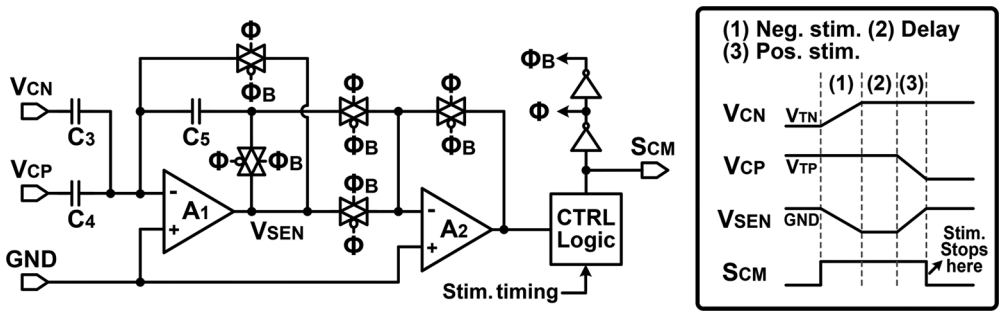

Fig. 5. Schematic diagram of the charge monitoring circuit.

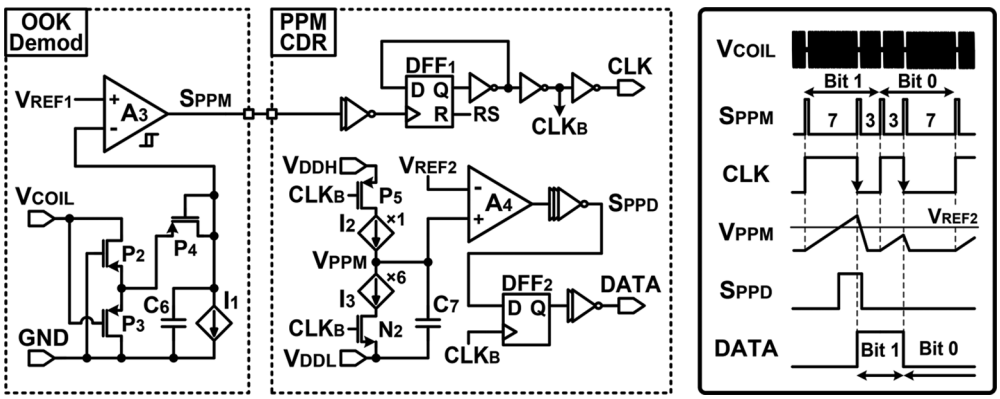

Fig. 6. Schematic diagrams of the on-off-keying (OOK) demodulator and pulse-position-modulated (PPM) clock and data recovery (CDR) circuits.

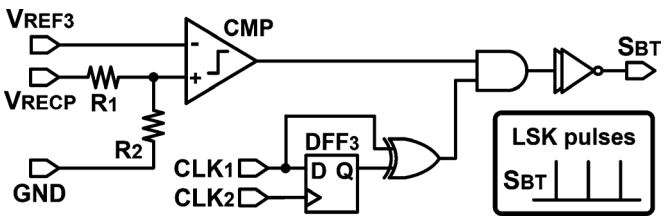

Fig. 7. Schematic diagrams of the V_{REC} sensing block for LSK back telemetry.

voltages at desired levels in the presence of coil misalignments and distance variations.

IV. Measurement Results

A. Chip Micrograph and Measured Waveforms

The 4-channel wireless SCS system was fabricated in the TSMC 0.35 μm 4M2P standard CMOS process, occupying 12 mm^2 including pads. Fig. 8 shows the chip micrograph and floor plan. According to [1], typical DBS parameters for voltage, pulse width, and frequency are 1–3.5 V, 60–210 μs, and 130–185 Hz, respectively. We designed the SCS system to have larger range of pulse width and frequency, 16–512 μs and 7.6–244 Hz, respectively, to enable more flexible therapies, while the peak stimulus voltage is limited to ± 2 V due to process constraints. Similar to commercial DBS devices, such as Activa from Medtronic (Minneapolis, MN), the SCS system has 4 stimulation channels with 4 pairs of off-chip capacitors (1 μF, $1 \times 0.5 \times 0.5$ mm^3 each), which are small enough to be placed on the opposite side of the chip to minimize the prototype dimensions. The storage capacitance of 1 μF was chosen to allow 4 pairs of capacitors to be fully charged at 244 Hz and each transfer charge up to 1.8 μC to the target tissue [1].

Measured waveforms in Fig. 9 show the operation of the charge monitoring (CM) circuit while changing the storage capacitor voltages, V_{CP1} and V_{CN1}, and the cathodic phase period, T_N. A cathodic-first biphasic stimulation voltage, V_{STIM}, flows through a series RC model (500 Ω and 1 μF) for the DBS application [9], [23]. In Fig. 9(a), the cathodic stimulation is applied for a predefined T_N of 512 μs with a capacitor pair charged to ± 2 V, discharging V_{CN1} by 850 mV. The anodic period, T_P, is then dynamically adjusted to 228 μs by the charge monitoring circuit, discharging the same amount of ΔV_{CP1} to ensure that injected and withdrawn charges are neutralized. Similarly, when T_N is 256 μs with a capacitor pair charged to ± 0.45 V in Fig. 9(b), the anodic phase lasts for T_P of 172 μs to discharge V_{CP1} by 150 mV, satisfying the charge balancing requirement.

Fig. 10 shows the overall SCS waveforms focusing on stimulation with different number of storage capacitor pairs. In Fig. 10(a), one capacitor pair charged to ± 2 V provides the stimulation current, I_{STIM}, with a decaying exponential shape. The stimulus amplitude (4 mA) and time constant (250 μs) depend on the storage capacitors (1 μF), electrodes/tissue time constant ($R_S = 500\,\Omega$ and $C_{DL} = 1\,\mu$F), and target$V_{CP,N}$ (± 2 V), as included in (4). With four capacitor pairs in Fig. 10(b), the time constant of I_{STIM} increases to 400 μs, resulting in a smaller discharged voltage (280 mV) from each capacitor. It should be noted that adjusting the number of storage capacitors can control the time constant of stimulus waveforms, while it

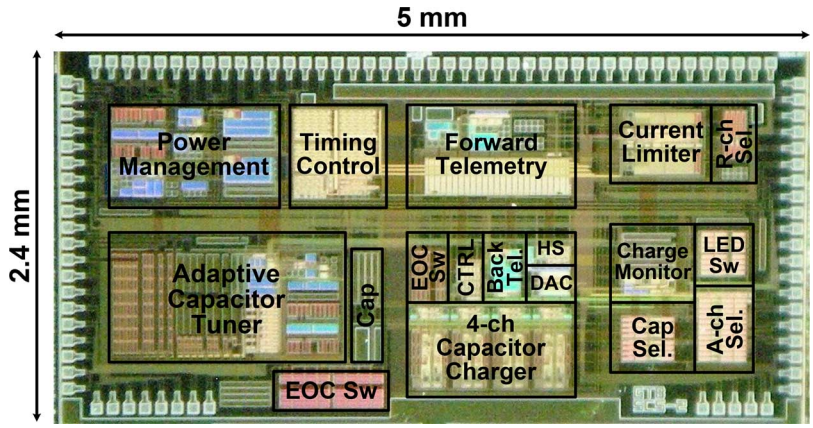

Fig. 8. Fabricated chip micrograph of the wireless SCS system in the TSMC 0.35 μm standard CMOS process.

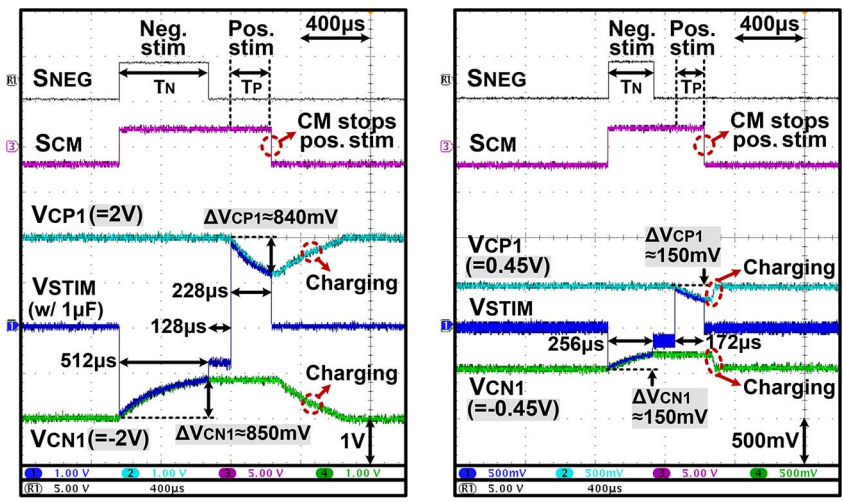

(a) (b)

Fig. 9. Measured waveforms of the charge monitoring circuit with (a) $V_{CP1} = 2$ V, $V_{CN1} = -2$ V, and $T_N = 512\,\mu$s and (b) $V_{CP1} = 0.45$ V, $V_{CN1} = -0.45$ V, and $T_N = 256\,\mu$s.

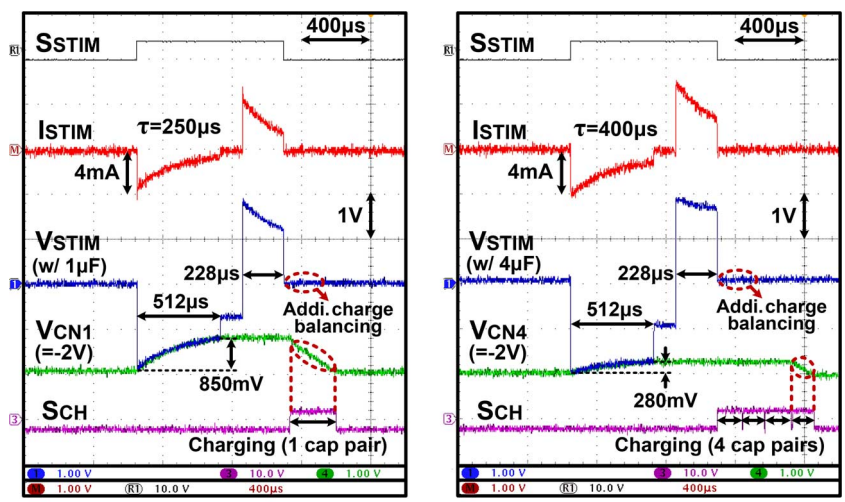

(a) (b)

Fig. 10. Measured waveforms of the overall SCS system, demonstrating the differences between stimulation with (a) one 1 μF capacitor pair and (b) four 1 μF capacitor pairs.

can limit simultaneous stimulation over multiple electrodes. After stimulation, capacitor pairs are sequentially recharged to their target voltages, while the site is shorted to *GND* during a predefined period for additional charge balancing.

Fig. 11 shows the measured waveforms of forward/back data telemetry. In Fig. 11(a), V_{COIL} is OOK-modulated on the Tx side to become the pulse-position-modulated carrier signal, S_{PPM}, which is recovered into synchronized 15.6 kbps

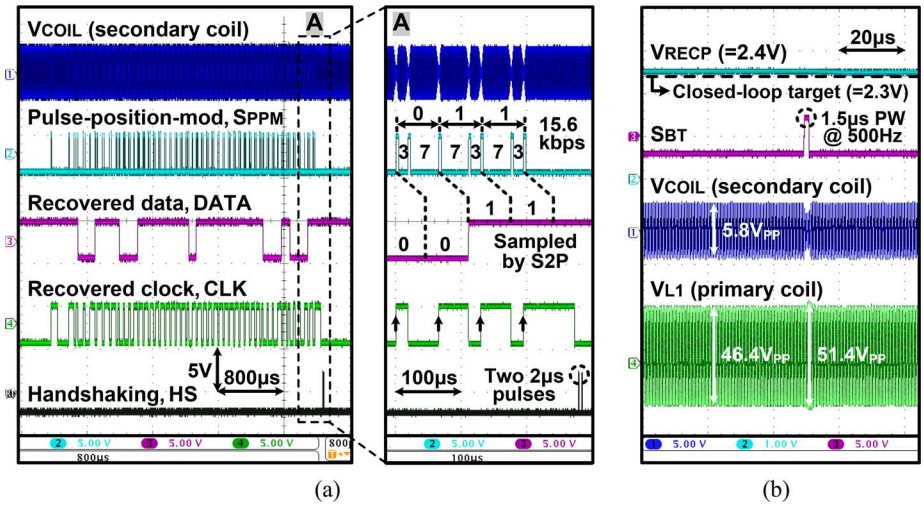

(a) (b)

Fig. 11. Measured waveforms of (a) the forward data telemetry and (b) back telemetry blocks.

data and clock signals by the PPM-CDR block on the Rx side. The recovered 40 bit data frames are sampled by S2P and stored in shift registers. After receiving the forward data, the handshaking block generates two short pulses (2 μs), which are provided to the external power Tx through LSK back telemetry. Fig. 11(b) shows the closed-loop power control capability with LSK back telemetry. When the positive rectifier output voltage, V_{RECP}, exceeds the closed-loop target voltage of 2.3 V, the V_{REC} sensing block provides a back telemetry signal, S_{BT}, with 1.5 μs pulse width at 500 Hz to close the LSK switch across L_2. The sudden drop in V_{COIL} and increment in the secondary quality factor, Q_2, result in the primary coil voltage to increase by 5 V_{PP}, which is detected by the LSK sensing block.

B. Charge Monitoring and Capacitor Charging

In order to verify the accuracy of the charge monitoring circuit, we measured the discharged voltage mismatch between negative and positive capacitors, C_N and C_P, for biphasic stimulation while calculating the residual charge in the tissue. Fig. 12(a) shows the measured discharged voltage of C_N, ΔV_{CN}, and the mismatch between discharged voltages of C_N and C_P, ΔV_{CN} - $|\Delta V_{CP}|$, during stimulation, while sweeping capacitor voltages, V_{CP} and V_{CN}, from $\pm$0.45 V to $\pm$2 V. We have tested three chips, which showed similar performance. The discharged voltage mismatch from the chip with median values was measured between 14 mV and 22 mV. Fig. 12(b) shows the calculated residual charge, ΔQ_{STIM}, vs. $V_{CP,N}$ in the tissue after stimulation, which is derived from

$$\Delta Q_{STIM} = |Q_{NEG}| - Q_{POS} = |C_N \Delta V_{CN}| - C_P \Delta V_{CP} \quad (5)$$

where Q_{NEG} and Q_{POS} are the injected and withdrawn charges during negative and positive stimulation, respectively, calculated from the measured discharged voltages, ΔV_{CN} and ΔV_{CP} in Fig. 12(a), while C_N and C_P are assumed to be 1 μF. The maximum residual charge is 22 nC with a cathodic phase period

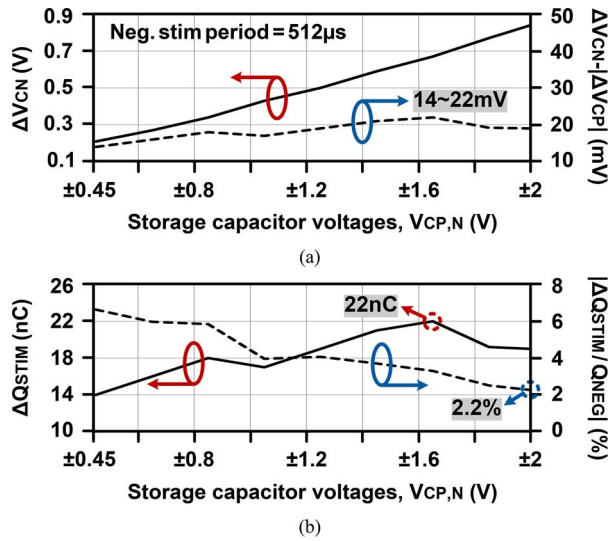

(a)

(b)

Fig. 12. (a) Measured discharged voltage of the negative capacitor, ΔV_{CN}, and discharged voltage mismatch between the negative and positive capacitors, $\Delta V_{CN} - \Delta V_{CP}$, for biphasic stimulation, (b) Calculated residual charge, $\Delta Q_{STIM} = |Q_{NEG}| - Q_{POS}$, in the tissue vs. peak capacitor voltage, $V_{CP,N}$.

of 512 μs, and the minimum charge ratio between ΔQ_{STIM} and Q_{NEG} is 2.2% when $V_{CP,N}$ are $\pm$2 V.

The residual charge of 22 nC results in the residual voltage of 22 mV after stimulation in the electrode/tissue model (series 500 Ω and 1 μF), which is well below the safety potential window of $\pm$100 mV [19]. It should be noted that mismatch between storage capacitors also affects the residual charge. For example, the 1-μF capacitors charged to $\pm$2 V discharge 850 mV for 512 μs in Fig. 12(a), injecting $\pm$850 nC. In this case, a 5% mismatch between commercial off-chip capacitors can lead to additional residual charge and voltage of 42.5 nC and 42.5 mV, respectively. While the total residual voltage in the worst case is still less than the safety window, the passive charge balancing circuit further discharges the residual voltage after stimulation to prevent any charge accumulation over long-term stimulation.

TABLE I
BENCHMARKING INDUCTIVELY-POWERED STIMULATING SYSTEMS

Publication		2010 [8]	2012 [9]	2011 [24]	**This work**
Technology		0.18-µm HV	0.35-µm	1.5-µm	**0.35-µm**
Stimulator structure		CCS	VCS + CCS	SCS	**SCS**
Supply voltage (V)		±12	3.3	±1.75 (Cap)	**±2 (Cap)**
Stimulator power efficiency (%)	Rec. + Reg.	85.6	80*	-	**-**
	DC-DC conv.	-	55 ~ 94	-	**-**
	Current driver	41.6	-	-	**-**
	Charger + Sw.	-	-	40**	**80.4**
	Total	35.6	44 ~ 75.2	40	**80.4**
Current stimulus shape		Rectangular	Rectangular	Decaying exponential	**Decaying exponential**
Max. I_{STIM} (mA)		0.5	0.45	0.4 (peak)	**4 (peak)**
Series *RC* model		10kΩ + 100nF	1kΩ + 0.93µF	1.15kΩ + 1µF	**0.5kΩ + 1µF**

* Assuming a rectifier is needed, ** including power consumption of the other blocks.

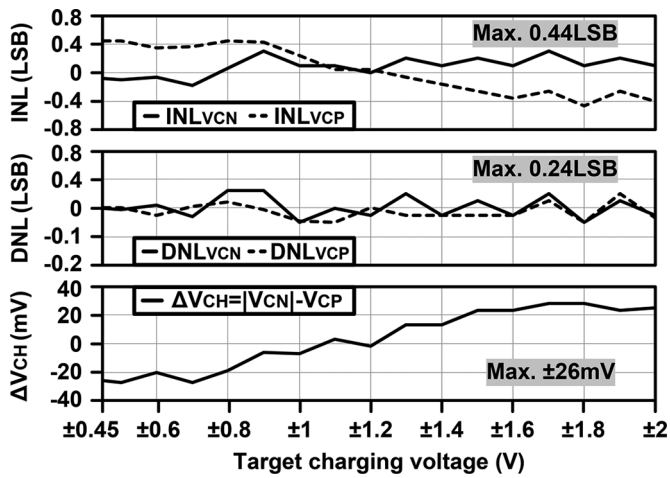

Fig. 13. Measured INL and DNL of the 5 bit storage capacitor peak voltages, V_{CN} and V_{CP}, along with the charging voltage mismatch, $\Delta V_{CH} = |V_{CN}| - V_{CP}$, between the negative and positive storage capacitors.

INL and DNL of the 5 bit storage capacitor voltages, V_{CP} and V_{CN}, with dual-control inductive capacitor charging were measured and presented in Fig. 13 along with the charged capacitor voltage mismatch, $\Delta V_{CH} = |V_{CN}| - V_{CP}$. While V_{CP} and V_{CN} are charged from ±0.45 V to ±2 V with 5 bit resolution, the maximum INL and DNL are 0.44 LSB and 0.24 LSB, respectively. The maximum ΔV_{CH} between $|V_{CN}|$ and V_{CP} is ±26 mV.

C. Performance Comparison and Summary

Table I benchmarks the current wireless SCS system prototype against state-of-the-art stimulating systems in the literature. Inductively-powered stimulating systems, which utilize CCS or VCS, require the rectifier, regulator, current driver, and even DC-DC converter blocks to generate rectangular stimuli, while power losses at each stage result in poor stimulator efficiencies. The stimulating system in [24] adopts switched-capacitor stimulation to construct rectangular stimuli with decaying exponential pulses, but it suffers from poor voltage-based capacitor charging efficiency ($<50\%$). Thanks to the efficient inductive capacitor charger and low-resistance capacitor/channel selectors, the wireless SCS system prototype is able to achieve capacitor charging efficiency of 82% and charge transfer efficiency of 98% when capacitor pairs are charged to ±2 V and provide decaying exponential stimuli to the tissue, respectively, resulting in overall stimulator efficiency of 80.4%. The power losses of the capacitor charger mainly result from the charger switches (14%), P_1 and N_1, and other charging circuitry (4%) such as switched drivers, $\mathrm{DRV_P}$ and $\mathrm{DRV_N}$, and the adaptive capacitor tuner in Fig. 3.

The SCS system offers flexible decaying exponential waveforms by adjusting stimulation parameters through forward telemetry, while the injected and withdrawn charges are continuously monitored and balanced for safe stimulation. For more flexible stimulus waveforms, the SCS system can be programmed to charge storage capacitors to various voltages and sequentially connect them to the stimulating site, generating a pseudo rectangular or ramp stimulus [24]. The number of off-chip storage capacitors may limit the waveform resolution though. Table II summarizes the specifications of the 4-channel wireless SCS system prototype.

V. ENERGY-EFFICIENT STIMULUS WAVEFORM EXPERIMENTS

A. Tissue Model Simulation

A decaying exponential stimulus is proven to be more effective in activating the neural tissue compared to rectangular and ramp stimuli, depending on the stimulus pulse width, while consuming the same amount of energy [11], [12]. The stimulus efficacy can be defined as the activated tissue area over stimulus energy. To verify the efficacy of stimulus waveforms, we created a simplified model of the neural tissue with uniformly distributed axons and stimulation electrodes for computer simulation, and compared the effects of stimulus waveforms on the area of tissue activated [25], [26].

Fig. 14 shows how different current stimulus waveforms affect the area of activated tissue when consuming the same

TABLE II
SPECIFICATIONS OF THE WIRELESS SCS SYSTEM PROTOTYPE

Overall System		**Switched-capacitor stimulation**	
L_1 / L_2 / f_C	4 µH / 1.2 µH / 2 MHz	# of channels	4 (active) + 4 (return)
ASIC area	12 mm^2	Stimulation freq.	7.6 ~ 244 Hz (5-bit) *
System supply	2.1 V / -2.1 V	Pulse width	16 ~ 512 µs (5-bit)*
Inductive capacitor charger		Charge balancing	Charge monitor + passive
Target voltages	±0.45 ~ ±2 V (5-bit)	$\|Q_{NEG}\|$ - Q_{POS}	< 22 nC w/ $C_{P,N}$ = 1 µF
INL / DNL	0.44 / 0.24 LSB	Current limiter	0.012 ~ 1.5mA (5-bit)**
$\|V_{CN}\|$ - V_{CP}	< ±26 mV	**Forward data telemetry**	
Charging eff. / time	45 ~ 82% / 40 ~ 420 µs	Data / Preamble	40 / 8 bits
C_S / $C_{P1\sim4}$ / $C_{N1\sim4}$	1 nF / 1 µF / 1 µF	PPM data rate	15.6 kbps

* Adjustable, ** Can be deactivated to allow higher current.

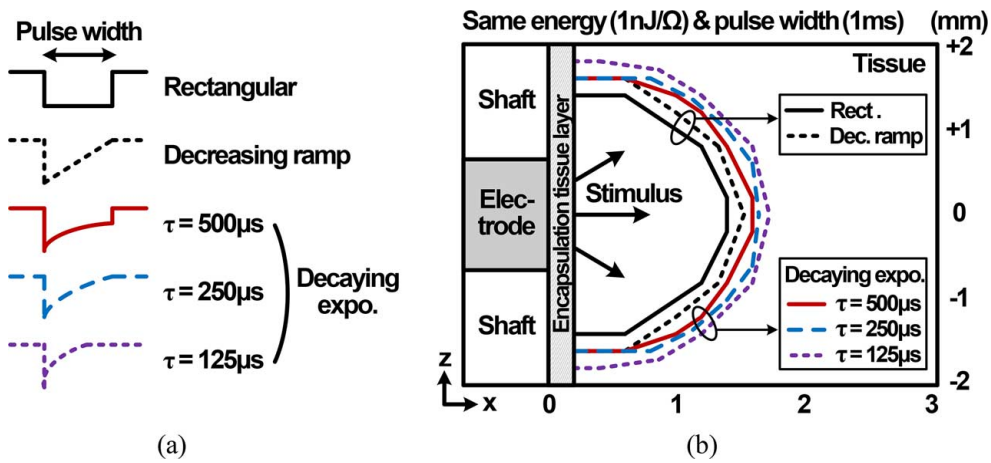

Fig. 14. (a) Several types of stimulus waveforms and (b) area of tissue activated by them when consuming the same amount of stimulus energy.

amount of energy for the same pulse width. The decaying exponential stimuli with different time constants (500 μs, 250 μs, and 125 μs) are applied to uniformly aligned axon arrays in the tissue model through the electrode along with the rectangular and decreasing ramp stimuli, as shown in Fig. 14(a). In this simulation, we assume that the axons in the tissue model are activated when their transmembrane potentials increase above a predefined threshold level with injected stimuli. In Fig. 14(b), the tissue model utilizes homogeneous isotropic tissue conductivity of 0.3 S/m and relative permittivity of 4×10^6 for frequencies below 250 Hz to include the effects of tissue resistance and capacitance in the brain [26], [27]. With the same stimulus energy (1 nJ/Ω) and pulse width (1 ms), the decaying exponential with smaller time constant can activate larger cross-sectional tissue area than the rectangular and decreasing ramp stimuli. In this case, the decaying exponential stimulus achieves 35–56% higher stimulus efficacy than the rectangular stimulus. In addition, further simulated results show that the decaying exponential stimulus can activate the same tissue area with less stimulus energy and injected charge than other stimulus waveforms when the pulse width is large (>0.4 ms), enabling both energy-efficient and safe stimulation. On the other hand, all waveforms show similar stimulus efficacies with small pulse width (<0.4 ms).

B. *In Vivo Experiments*

To demonstrate the charge-based stimulation capability of the SCS system, *in vivo* brain stimulation was conducted on an anesthetized cat after receiving the necessary approval from the Institutional Animal Care and Use Committee (IACUC) at Duke University. The SCS system provided decaying exponential stimulus pulses to the posterior limb of the internal capsule, while the electromyography (EMG) signals in the upper arm muscles, resulted from the evoked neural activities in the brain, were recorded. For brain stimulation, 30 biphasic-bipolar pulses at 244 Hz including a decaying exponential cathodic pulse for 272 μs followed by a current-limited charge-balancing anodic pulse for 1.1 ms were applied, while sweeping the cathodic stimulation amplitude from -0.4 V to -1.5 V. Fig. 15 shows the *in vivo* measured waveforms of the current stimulus and EMG voltage response when storage capacitors of 1 μF were charged to ± 1.5 V. With the current stimulus resembling a decaying exponential shape, R_S and C_{DL} of the electrode and tissue interface were approximated as 560 Ω and 1.9 μF, respectively, resulting in the peak amplitude of -2.68 mA and time constant of 367 μs. The measured EMG voltage was rectified and integrated to quantify the EMG response with respect to the stimulus amplitude.

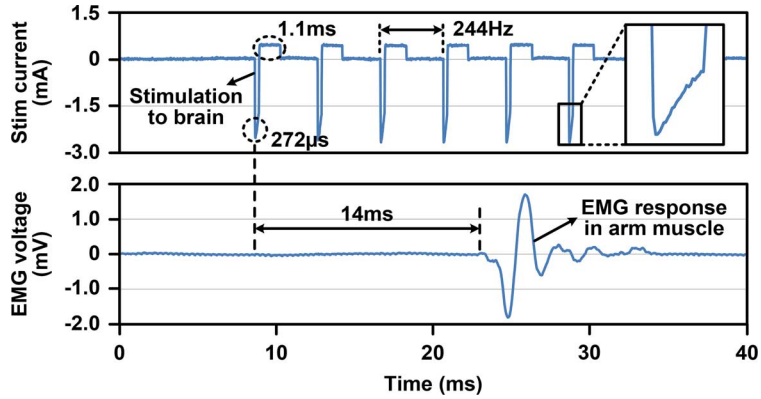

Fig. 15. *In vivo* measured waveforms of the decaying exponential current stimulus and EMG voltage response.

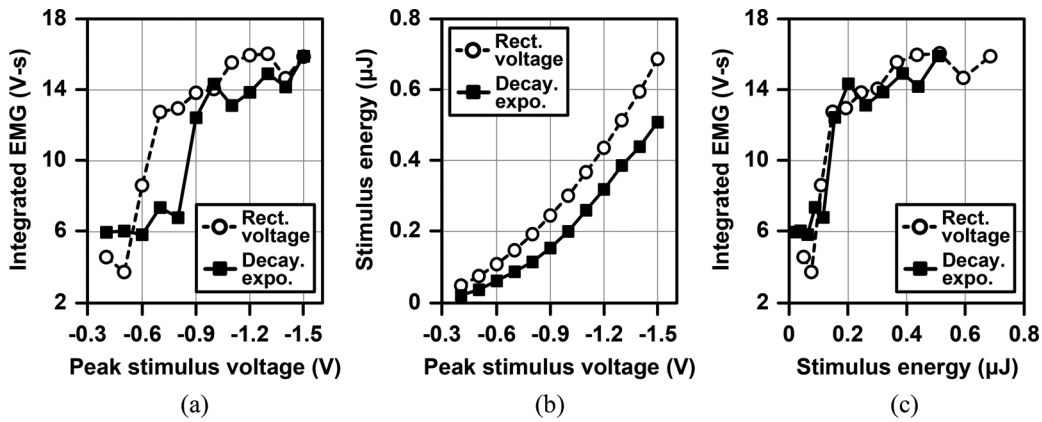

Fig. 16. *In vivo* experimental results with decaying exponential and rectangular stimulus pulses. (a) Integrated EMG voltage vs. peak stimulus voltage, (b) stimulus energy vs. peak stimulus voltage, and (c) integrated EMG voltage vs. stimulus energy.

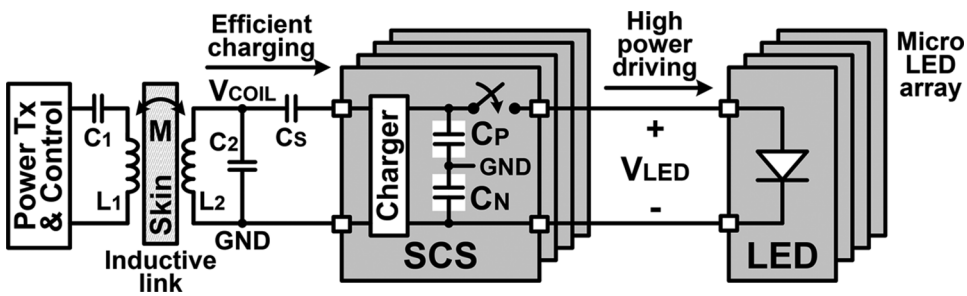

Fig. 17. Conceptual diagram of the wireless SCS system for power-efficient optogenetics by driving an array of micro-LEDs.

Fig. 16 shows how the decaying exponential stimulus affects the overall efficacy of stimulation when compared to the conventional rectangular stimulus. In Fig. 16(a), the rectified and integrated EMG voltages over time start increasing after the stimulus voltage goes above a certain threshold, and the decaying exponential requires a higher peak voltage. However, the decaying exponential stimulus has lower stimulus energy than the rectangular stimulus at the same peak voltage, as shown in Fig. 16(b). Therefore, when consuming the same amount of stimulus energy in Fig. 16(c), the EMG responses of both stimulus waveforms become closer, leading to similar stimulus efficacies. In this case, higher stimulator efficiency of the SCS architecture further improves the overall efficiency of the wireless stimulators with the decaying exponential stimulus.

VI. Power-Efficient Wireless Optogenetic Experiments

A. Wireless Optogenetics With SCS

The proposed SCS system is capable of providing high instantaneous current from storage capacitors without affecting the inductive link and system supply voltages, which are the limiting factors for the optogenetic applications in conventional inductively-powered implantable devices. For example, a micro-LED in [28] consumes 17 mW at 2.9 V to instantaneously provide sufficient irradiance of 10 mW/mm^2 for neural activation. This dramatic change in load current can significantly drop the receiver coil voltage in a conventional inductively-powered stimulator, and it is even more critical in simultaneous multi-channel optogenetic stimulation. We have

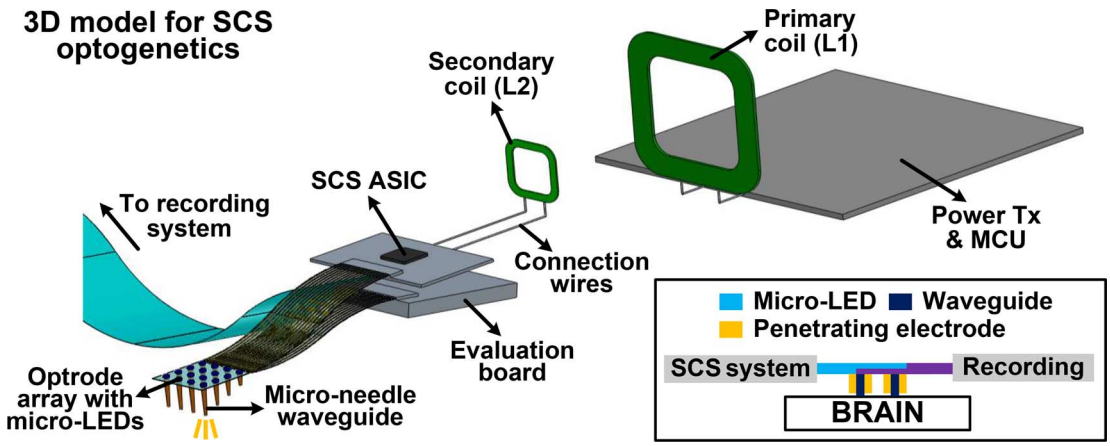

Fig. 18. 3-D test setup model for our *in vivo* optogenetic experiment with the SCS system prototype. Inset: Simplified diagram of the optrode array with micro-LEDs for optical stimulation and penetrating electrodes for simultaneous neural recording.

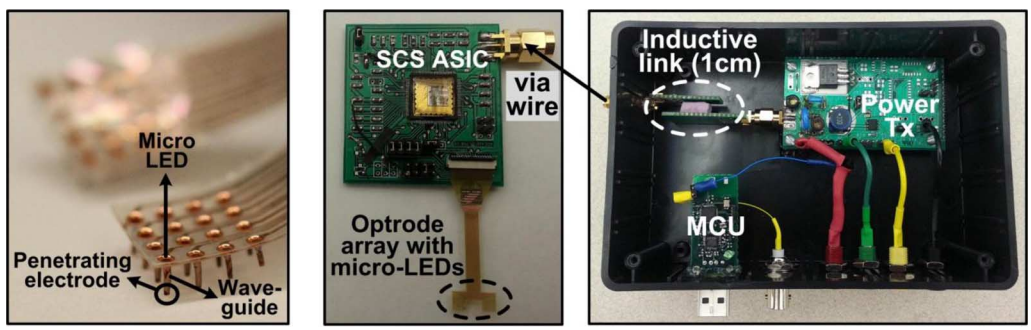

Fig. 19. Optogenetics test setup components including, (a) the 3-D optrode array with waveguides, (b) the SCS system prototype, and (c) the external electronics for the power Tx and inductive link consisting of a pair of perfectly-aligned planar spiral coils at 1 cm separation.

demonstrated the utility of the SCS system for power-efficient wireless optogenetics by periodically discharging the storage capacitors into micro-LED arrays, which requires high instantaneous power to emit sufficient light and evoke the neural activity [29]. Fig. 17 shows the conceptual diagram of the wireless SCS system which efficiently charges storage capacitors, C_P and C_N, while being capable of driving micro-LEDs with high instantaneous current. Unlike the conventional wireless optical stimulator in [15], which suffers from power losses across a rectifier, a regulator, and an LED driver, the SCS system utilizes the efficient capacitor charger and its instantaneous charge transfer capability to drive the LEDs, improving the optical stimulator power efficiency. After charging, C_P and C_N pairs are connected in series to provide higher LED voltage, V_{LED}, for optical stimulation.

Fig. 18 shows the 3-D test setup model for *in vivo* wireless optogenetics with the SCS system which receives wireless power and data through the inductive link. The SCS ASIC drives the 3-D flexible optrode array, which consists of micro-LEDs for optical stimulation and penetrating electrodes for neural recording as shown in Fig. 18 [28]. Micro-needle waveguides that are made out of transparent SU8 polymer using micromachining technology enable precise and efficient light delivery to the target tissue with high spatial resolution. The neural signals are recorded with a commercial setup (RHD2132, Intan Technologies, Los Angeles, CA, USA) from the penetrating electrodes, which are wrapped around the waveguide core and only exposed at the tips of the waveguides. As a result, the wireless SCS system combined with slanted optrode arrays enables simultaneous optical stimulation and electrical neural recording for an untethered bi-directional neural interface.

B. In Vivo Optogenetics Experiments

In order to verify the capability of power-efficient optogenetics with the SCS system, *in vivo* acute animal experiments were performed with the optrode array and additional recording setup in Fig. 18. For optogenetic animal experiments, Sprague-Dawley rats were virally transfected with channelrhodopsin-2 (ChR2) to make them light sensitive [30]. In the optrode array, each surface-mounted micro-LED (TR2227TM, Cree Inc., Durham, NC, USA), which occupies $220 \times 270 \times 50$ μm^3 area and has a peak at 460 nm wavelength, was coupled with the 1.2-mm-long waveguides that included the penetrating electrodes around them. Fig. 19 shows the optogenetics test setup including the 3-D optrode array with waveguides, the SCS system, and the external power Tx with the inductive link. Fig. 20 shows the *in vivo* setup for optogenetic experiment in the visual cortex (V1) of an anesthetized rat using the SCS system. The inductive link provides wireless power and data to the SCS system via a twisted pair of interconnecting wires from the Rx coil. The SCS provides high instantaneous power to the LEDs, generating and delivering

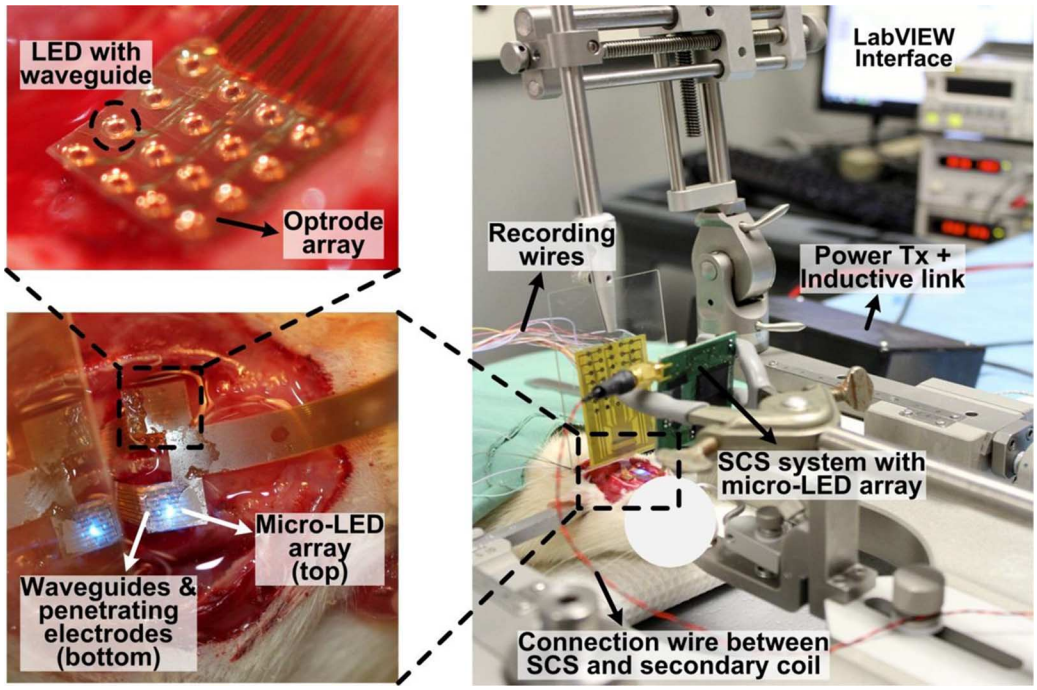

Fig. 20. *In vivo* optogenetic experimental setup on an anesthetized viral-transfected rat using the SCS system prototype, shown in Fig. 18.

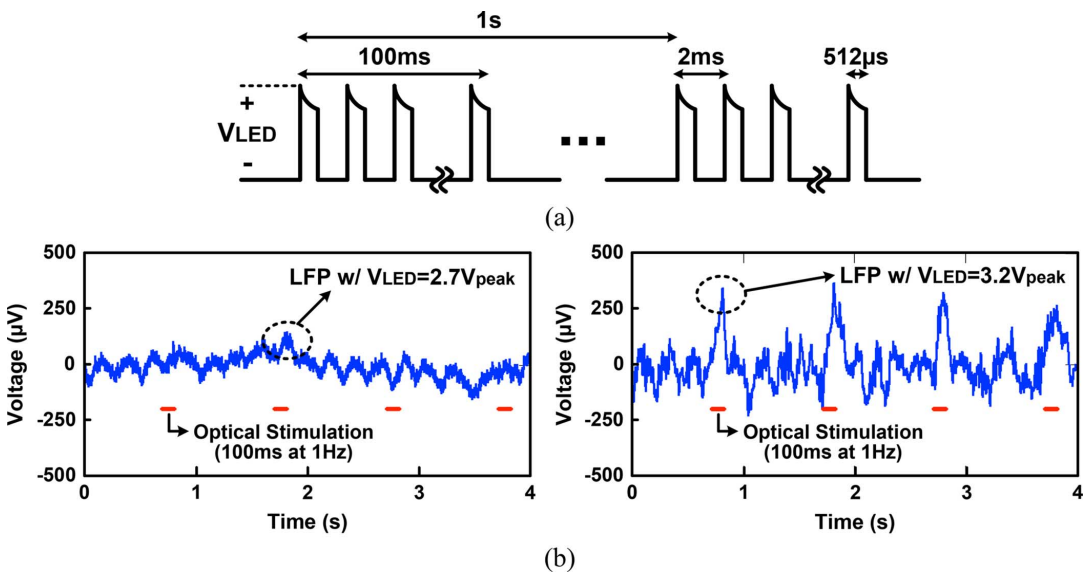

Fig. 21. (a) The LED driving voltage, V_{LED}, for *in vivo* optogenetics with SCS, (b) The difference between light-induced local field potentials (LFP) with $V_{LED} = 2.7\,V_{\text{peak}}$ (below stimulation threshold) and $V_{LED} = 3.2\,V_{\text{peak}}$ (above stimulation threshold).

light to the selective target areas in the visual cortex through micro-needle waveguides.

Fig. 21 shows the LED driving voltage, V_{LED}, for optical stimulation with SCS and simultaneously recorded light-induced *in vivo* local field potentials (LFP). The LFPs below 500 Hz were recorded using the optrode array with waveguides in the neural tissue when the SCS system drove micro-LEDs with a 512 μs pulse train of 100 ms wide at 1 Hz and V_{LED} of 2.7 V_{peak} and 3.2 V_{peak}, as shown in Fig. 21(a). While no significant neural modulation is observed with V_{LED} of 2.7 V_{peak}, the higher V_{LED} of 3.2 V_{peak} results in the micro-LEDs to deliver sufficient irradiance through the waveguides for observing light-evoked neural response in the target tissue. This in turn leads to larger LFP variations, as shown in Fig. 21(b), verifying the efficacy of the wireless optical stimulation by the SCS system.

Average irradiance of the LED was measured and presented in Fig. 22 when driven by rectangular pulses from a signal generator vs. decaying exponential pulses from the wireless SCS system, while sweeping the peak LED voltage. The LED optical power was measured with an optical power meter (Newport Series 815, Irvine, CA) and divided by the LED surface area (0.19×0.24 μm^2) to calculate irradiance. In Fig. 22(a), the rectangular pulse with V_{LED} of 3.2 V leads to the irradi-

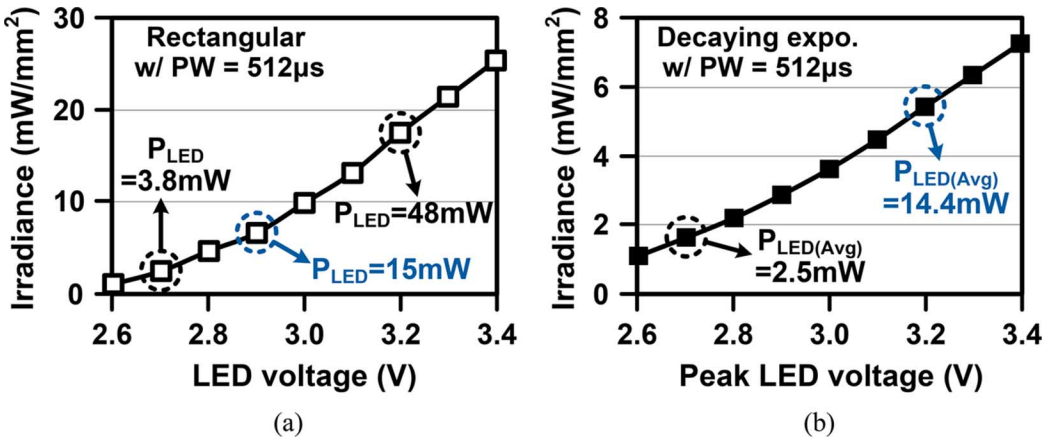

Fig. 22. Measured irradiance of the LED when it is driven by (a) rectangular pulses from a signal generator and (b) decaying exponential pulses from the wireless SCS system, vs. the peak LED voltage.

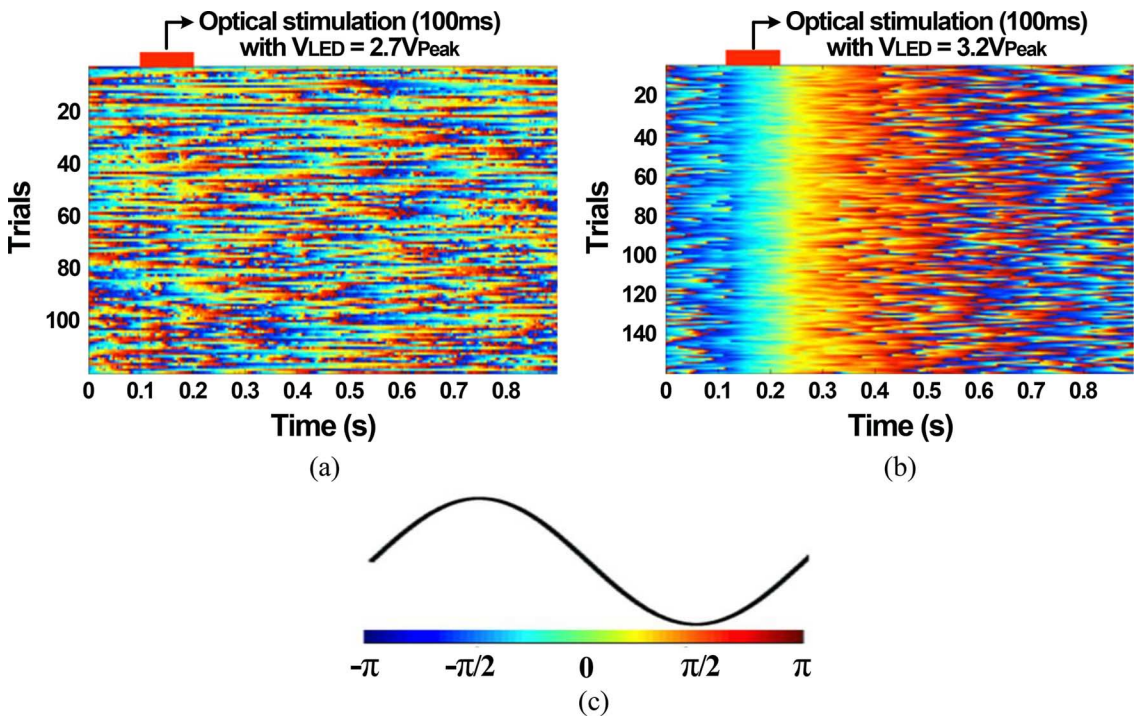

Fig. 23. Instantaneous phase of light-evoked LFPs at low frequency band (1–25 Hz) with (a) $V_{LED} = 2.7\,V_{\rm peak}$ (below threshold) and (b) $V_{LED} = 3.2\,V_{\rm peak}$ (above threshold). (c) Corresponding color coding.

ance of 17.5 mW/mm^2, requiring 48 mW to be delivered to the LED. On the other hands, the decaying exponential pulse with V_{LED} of 3.2 $V_{\rm peak}$ in Fig. 22(b) delivers 14.4 mW to the LED within 512 μs, resulting in 5.6 mW/mm^2 irradiance, sufficient to evoke the light-induced LFP in Fig. 21. A rectangular pulse with smaller V_{LED} of 2.9 V generates a similar irradiance of 6.3 mW/mm^2, by delivering 15 mW to the LED, which would still be difficult to provide in conventional implantable stimulators. In addition, the irradiance also shows a decaying exponential shape over time because it is proportional to the decaying exponential input current of LEDs.

To visualize neural oscillations generated by the SCS system and optrode arrays, we measured instantaneous phases of the light-induced LFPs with V_{LED} of 2.7 $V_{\rm peak}$ and 3.2 $V_{\rm peak}$ within 1–25 Hz based on Hilbert Transform, as shown in Fig. 23. The instantaneous phases of each trial are labeled with the color coding in Fig. 23(c), while the SCS system provides 100 ms optical stimulation at 1 Hz. In Fig. 23(a), no phase consistency is observed in the neural recording because the micro-LEDs driven with V_{LED} of 2.7 $V_{\rm peak}$ do not reach sufficient irradiance to induce optogenetic stimulation in the target tissue. On the other hand, the light-induced LFPs with V_{LED} of 3.2 $V_{\rm peak}$ in Fig. 23(b) show clear synchronization of instantaneous phases over multiple trials, which are aligned based on each optical stimulation period.

VII. Conclusion

We have developed a wireless switched-capacitor based stimulating (SCS) system, which offers high efficiency, high driving capability, and safety for both electrical and optical

deep brain stimulation. The proposed SCS system efficiently charges pairs of storage capacitor directly from the inductive link through a dual-control inductive capacitor charger, while alternately connecting negative and positive capacitors to the electrodes for charge-based stimulation, leading to high stimulator efficiency (before the electrode). A charge monitoring circuit measures the amount of charge injected and withdrawn, and adaptively changes the stimulus pulse width to neutralize the residual charge in the tissue, ensuring charge balancing. The SCS system also utilizes OOK-PPM forward data telemetry and LSK back telemetry for robust bi-directional wireless data communication, while an on-chip timing controller and power management unit create the fully-integrated wireless SCS system-on-a-chip.

We have demonstrated through stimulus efficacy simulations that a decaying exponential stimulus, which is normally generated by the proposed SCS architecture, requires smaller or at least similar stimulus energy and injected charge to activate the same tissue area compared to the conventional rectangular stimulus, improving the stimulus efficacy (after the electrode). We also utilize the SCS system in power-efficient wireless optogenetics because of its high instantaneous power driving capability. *In vivo* experimental results verify the feasibility and efficacy of both electrical and optical stimulation using the SCS system prototype.

ACKNOWLEDGMENT

The authors would like to thank Prof. Warren M. Grill and Bryan Howell in the Biomedical Engineering Department at Duke University for their help in comparing the SCS and conventional stimulating systems for neural stimulation experiments on cats.

REFERENCES

[1] A. M. Kuncel and W. M. Grill, "Selection of stimulus parameters for deep brain stimulation," *Clin. Neurophysiol.*, vol. 115, no. 11, pp. 2431–2441, Nov. 2004.

[2] D. R. Merrill, M. Bikson, and J. G. R. Jefferys, "Electrical stimulation of excitable tissue: Design of efficacious and safe protocols," *J. Neuroscience Methods*, vol. 141, pp. 171–198, Feb. 2005.

[3] S. K. Moore, "Psychiatry's shocking new tools," *IEEE Spectrum*, vol. 43, no. 3, pp. 24–31, Mar. 2006.

[4] B. S. Wilson and M. F. Dorman, "Cochlear implants: A remarkable past and a brilliant future," *Hearing Res.*, vol. 242, no. 1-2, pp. 3–21, Aug. 2008.

[5] H.-M. Lee, H. Park, and M. Ghovanloo, "A power-efficient wireless system with adaptive supply control for deep brain stimulation," *IEEE J. Solid-State Circuits*, vol. 48, no. 9, pp. 2203–2216, Sep. 2013.

[6] J. Vidal and M. Ghovanloo, "Toward a switched-capacitor based stimulator for efficient deep-brain stimulation," in *Proc. IEEE Eng. in Med. and Biol. Conf. (EMBC)*, Sep. 2010, pp. 2927–2930.

[7] J. Simpson and M. Ghovanloo, "An experimental study of voltage, current, and charge controlled stimulation front-end circuitry," in *Proc. IEEE Int. Symp. Circuits Syst. (ISCAS)*, May 2007, pp. 325–328.

[8] K. Chen, Z. Yang, L. Hoang, J. Weiland, M. Humayun, and W. Liu, "An integrated 256-channel epiretinal prosthesis," *IEEE J. Solid-State Circuits*, vol. 45, no. 9, pp. 1946–1956, Sep. 2010.

[9] S. Arfin and R. Sarpeshkar, "An energy-efficient, adiabatic electrode stimulator with inductive energy recycling and feedback current regulation," *IEEE Trans. Biomed. Circuits Syst.*, vol. 6, no. 1, pp. 1–14, Feb. 2012.

[10] M. Ghovanloo, "Switched-capacitor based implantable low-power wireless microstimulating systems," in *Proc. IEEE Int. Symp. Circuits Syst. (ISCAS)*, May 2006, pp. 2197–2200.

[11] A. Wongsarnpigoon, J. P. Woock, and W. M. Grill, "Efficiency analysis of waveform shape for electrical excitation of nerve fibers," *IEEE Trans. Neural. Syst. Rehab. Eng.*, vol. 18, no. 3, pp. 319–328, Jun. 2010.

[12] A. Wongsarnpigoon and W. M. Grill, "Energy-efficient waveform shapes for neural stimulation revealed with a genetic algorithm," *J. Neural. Eng.*, vol. 7, no. 4, Jun. 2010.

[13] F. Zhang, A. Aravanis, A. Adamantidis, L. de Lecea, and K. Deisseroth, "Circuit-breakers: Optical technologies for probing neural signals and systems," *Nature Reviews Neuroscience*, vol. 8, no. 8, pp. 577–581, Aug. 2007.

[14] V. Gilja *et al.*, "Challenges and opportunities for next-generation intracortically based neural prostheses," *IEEE Trans. Biomed. Eng.*, vol. 58, no. 7, pp. 1891–1899, Jul. 2011.

[15] C. T. Wentz, J. G. Bernstein, P. Monahan, A. Guerra, A. Rodriguez, and E. S. Boyden, "A wirelessly powered and controlled device for optical neural control of freely-behaving animals," *J. Neural. Eng.*, vol. 8, no. 4, Jun. 2011.

[16] M. Kiani, U. Jow, and M. Ghovanloo, "Design and optimization of a 3-coil inductive link for efficient wireless power transmission," *IEEE Trans. Biomed. Circuits Syst.*, vol. 5, no. 6, pp. 579–591, Dec. 2011.

[17] H.-M. Lee, K.-Y. Kwon, W. Li, and M. Ghovanloo, "A power-efficient switched-capacitor stimulating system for electrical/optical deep-brain stimulation," in *IEEE Int. Solid-State Circuits Conf. (ISSCC)*, Feb. 2014, pp. 414–415.

[18] M. Kiani and M. Ghovanloo, "An RFID-based closed loop wireless power transmission system for biomedical applications," *IEEE Trans. Circuits Syst. II*, vol. 57, no. 4, pp. 260–264, Apr. 2010.

[19] K. Sooksood, T. Stieglitz, and M. Ortmanns, "An active approach for charge balancing in functional electrical stimulation," *IEEE Trans. Biomed. Circuits Syst.*, vol. 4, no. 3, pp. 162–170, Jun. 2010.

[20] J.-J. Sit and R. Sarpeshkar, "A low-power blocking-capacitor-free charge-balanced electrode-stimulator chip with less than 6 nA dc error for 1-mA full-scale stimulation," *IEEE Trans. Biomed. Circuits Syst.*, vol. 1, no. 3, pp. 172–183, Sep. 2007.

[21] H.-M. Lee and M. Ghovanloo, "A power-efficient wireless capacitor charging system through an inductive link," *IEEE Trans. Circuits Syst. II*, vol. 60, no. 10, pp. 707–711, Oct. 2013.

[22] S. Paul, A. M. Schlaffer, and J. A. Nossek, "Optimal charging of capacitors," *IEEE Trans. Circuits Syst. I*, vol. 47, no. 7, pp. 1009–1016, Jul. 2000.

[23] X. F. Wei and W. M. Grill, "Impedance characteristics of deep brain stimulation electrodes *in vitro* and *in vivo*," *J. Neural. Eng.*, vol. 6, no. 4, Aug. 2009.

[24] S. Kelly and J. Wyatt, "A power-efficient neural tissue stimulator with energy recovery," *IEEE Trans. Biomed. Circuits Syst.*, vol. 5, no. 1, pp. 20–29, Feb. 2011.

[25] C. C. McIntyre, A. G. Richardson, and W. M. Grill, "Modeling the excitability of mammalian nerve fibers: Influence of afterpotentials on the recovery cycle," *J. Neurophysiol.*, vol. 87, no. 2, Feb. 2002.

[26] C. R. Butson and C. C. McIntyre, "Tissue and electrode capacitance reduce neural activation volumes during deep brain stimulation," *Clin. Neurophysiol.*, vol. 116, no. 10, pp. 2490–2500, Oct. 2005.

[27] S. Gabriel, R. W. Lau, and C. Gabriel, "The dielectric properties of biological tissues: II. Measurements in the frequency range 10 Hz to 20 GHz," *Phys. Med. Biol.*, vol. 41, no. 11, pp. 2251–2269, Nov. 1996.

[28] K. Kwon, A. Khomenko, M. Haq, and W. Li, "Integrated slanted microneedle-LED array for optogenetics," in *Proc. IEEE Eng. in Med. and Biol. Conf. (EMBC)*, Jul. 2013, pp. 249–252.

[29] K. Kwon, B. Sirowatka, A. J. Weber, and W. Li, "Opto-μECoG array: A hybrid neural interface with transparent μECoG electrode array and integrated LEDs for optogenetics," *IEEE Trans. Biomed. Circuits Syst.*, vol. 7, no. 5, pp. 593–600, Oct. 2013.

[30] F. Zhang, L.-P. Wang, E. S. Boyden, and K. Deisseroth, "Channelrhodopsin-2 and optical control of excitable cells," *Nat. Methods*, vol. 3, no. 10, pp. 785–792, Oct. 2006.

Hyung-Min Lee (S'06) received the B.S. degree in electrical engineering (*summa cum laude*) from Korea University, Seoul, Korea, in 2006, the M.S. degree in electrical engineering from the Korea Advanced Institute of Science and Technology (KAIST), Daejeon, Korea, in 2008, and the Ph.D. degree in electrical and computer engineering from Georgia Institute of Technology, Atlanta, GA, USA, in 2014.

He is currently a postdoctoral associate in the Department of Electrical Engineering and Computer Science, Massachusetts Institute of Technology (MIT), Cambridge, MA, USA. His research interests include analog/mixed-signal/power-management integrated circuit and system design for implantable biomedical applications.

Dr. Lee received Silver Prizes in the 16th and 18th Human-Tech Thesis Prize contest from Samsung Electronics, Korea, in 2010 and 2012, respectively, and the Commendation Award in the 4th Outstanding Student Research Award from TSMC, Taiwan, in 2010.

Ki Yong Kwon (S'09) received the B.S. and M.S. degree in electrical engineering from Michigan State University, East Lansing, MI, USA, in 2007 and 2010, respectively. He is currently pursuing the Ph.D. degree in electrical engineering at Michigan State University, East Lansing.

His research interests include neural interfaces, neurophysiological signal processing, and microsystem integration and packaging technologies.

Wen Li (S'03–M'09–SM'14) received the Ph.D. (2008) and M.S. (2004) in electrical engineering from the California Institute of Technology, Pasadena, CA, USA.

Dr. Li is currently an Assistant Professor of electrical and computer engineering at Michigan State University, East Lansing, MI, USA. Her research focuses on MEMS/NEMS, neuroprosthetic devices, micro/nano sensors and actuators, nanoelectronics, and microsystem integration and packaging technologies.

Maysam Ghovanloo (S'00–M'04–SM'10) received the B.S. degree in electrical engineering from the University of Tehran, Tehran, Iran, in 1994, the M.S. degree in biomedical engineering from the Amirkabir University of Technology, Tehran, Iran, in 1997, and the M.S. and Ph.D. degrees in electrical engineering from the University of Michigan, Ann Arbor, MI, USA, in 2003 and 2004, respectively.

From 2004 to 2007, he was an Assistant Professor in the Department of Electrical and Computer Engineering, North Carolina State University, Raleigh, NC, USA. He joined the faculty of the Georgia Institute of Technology, Atlanta, GA, USA, in 2007, where he is currently an Associate Professor and the Founding Director of the Georgia Tech Bionics Lab in the School of Electrical and Computer Engineering. He has authored or coauthored more than 150 conference and journal publications.

Dr. Ghovanloo is an Associate Editor of the IEEE TRANSACTIONS ON BIOMEDICAL CIRCUITS AND SYSTEMS and the IEEE TRANSACTIONS ON BIOMEDICAL ENGINEERING. He is the general chair of the 2015 IEEE Biomedical Circuits and Systems (BioCAS) Conference. He served on the IEEE International Solid-State Circuits Conference (ISSCC) subcommittee for imagers, MEMS, medical, and displays from 2010-2014. He has received awards in the 40th and 41st DAC/ISSCC Student Design Contests. He has organized special sessions and was a member of Technical Review Committees for several major conferences, such as ISSCC and ISCAS, in the areas of biomedical circuits, sensors, and systems. He is a member of the Tau Beta Pi, the Sigma Xi, and the IEEE Solid-State Circuits Society, the IEEE Circuits and Systems Society, and the IEEE Engineering in Medicine and Biology Society.